

Review

Numerical Modeling of Sperm Swimming

Fang-Bao Tian * and Li Wang 

School of Engineering and Information Technology, University of New South Wales, Canberra, ACT 2600, Australia; l.wang@unsw.edu.au

* Correspondence: f.tian@adfa.edu.au or onetfbao@gmail.com

Abstract: Due to rising human infertility, sperm motility has been an important subject. Among the hundreds of millions of sperms on the journey up the oviducts, only a few excellent travelers will reach the eggs. This journey is affected by many factors, some of which include sperm quality, sperm density, fluid rheology and chemotaxis. In addition, the sperm swimming through different body tracks and fluids involves complex sperm flagellar, complex fluid environment, and multi-sperm and sperm-wall interactions. Therefore, this topic has generated substantial research interest. In this paper, we present a review of computational studies on sperm swimming from an engineering perspective with focus on both simplified theoretical methods and fluid–structure interaction methods. Several open issues in this field are highlighted.

Keywords: sperm swimming; low Reynolds number; finite-boundary method; immersed boundary method; lattice Boltzmann method



Citation: Tian, F.-B.; Wang, L. Numerical Modeling of Sperm Swimming. *Fluids* **2021**, *6*, 73. <https://doi.org/10.3390/fluids6020073>

Academic Editor: Michael W. Plesniak

Received: 15 January 2021

Accepted: 5 February 2021

Published: 7 February 2021

Publisher's Note: MDPI stays neutral with regard to jurisdictional claims in published maps and institutional affiliations.



Copyright: © 2021 by the authors. Licensee MDPI, Basel, Switzerland. This article is an open access article distributed under the terms and conditions of the Creative Commons Attribution (CC BY) license (<https://creativecommons.org/licenses/by/4.0/>).

1. Introduction

“Life is like a journey” as stated by an anonymous philosopher. But in the case of living beings like mammals, life literally begins with a journey. It begins with a long journey of hundreds of millions of sperms, passing through the reproductive tracks of the female trying to reach the oviducts, with an ultimate aim to unite with one of the eggs. However, only a few excellent travelers will reach the eggs indicating the complexity of the flow paths and the environments experienced by the sperms. This remarkable journey has attracted growing interest over the past several decades [1–7], to understand the mechanisms used by the sperms to swim through different complex environments with the potential of using the findings to solve some of the significant problems faced nowadays like human infertility and to save some mammal species from extinction. Among the applications, solving human infertility can have a huge impact on the lives of many people. It is estimated that about 70 million couples around the world cannot conceive a child [8] due to infertility and that that nearly 7% of men is affected by infertility [9,10]. The male infertility is due to several factors such as low sperm count, low sperm quality, low sperm motility etc. In addition, it is also observed that the average sperm density has been decreasing during the past several decades [11]. Therefore it is desired to study the sperm swimming to achieve a better understanding of sperm motility.

There are different types of swimming organisms in nature ranging from large whales to micro-organisms like bacteria. Depending on their size and speed, these swimmers experience different types of flow regimes while swimming. For large creatures such as fishes, the inertial forces of the fluid are dominant while for micro organisms the viscous forces of the fluid plays a significant role. To correlate the inertial forces to the viscous forces of a fluid, an important non-dimensional parameter, Reynolds number (Re), is used and defined as,

$$\text{Re} = \frac{UL}{\nu}, \quad (1)$$

where ν is the kinematic viscosity of the fluid, U is the reference speed, and L is swimmer length. If numerical methods are used to study the fluid–structure interaction of swimmers,

the swimming speed is usually unknown, and determined by the fluid–structure interaction solver. In this case, the traveling wave speed is usually used as the reference speed [12], which defines a Reynolds number larger than the one defined by the forward swimming speed. Regarding sperm swimming, there are several factors that should be considered. In general, the sperm length is less than 100 μm, while the sperm speed is less than 200 μm/s [13]. Such parameters define a Reynolds number of $O(0.1)$ indicating that the sperm should swim in a special way different from larger and faster swimmers [3]. Considering the facts that the traveling wave speed is generally larger than the forward speed and that most body fluid is shear-thinning-like non-Newtonian fluid, the effective Reynolds number for sperm swimming could be of $O(1)$. In addition, the motion of ambient fluids should be taken into account as well, which in general have much higher velocities compared to the sperm speed. Therefore we can conclude that the flow regimes involved in sperm swimming cover both Stokes and laminar flows, which have been respectively covered by Lauga [14] and Childress [15].

The dominantly used strategy for a sperm swimming through a fluid is to make traveling wave (from head to tail) motion [7] and/or to improve its frequency so that $\sigma Re = O(1)$ (where σ is the ratio of lateral oscillating speed to the forward swimming speed) to break the time-reversal symmetry [16]. This is different from the large animals which use both traveling and flapping motions [12,17,18]. The traveling wave can be described by [19,20]

$$(x_0, y_0) = [x_0, A(x_0) \sin(2\pi(x_0 - ct)/\lambda)], \text{ for 2D,} \tag{2}$$

$$(x_0, y_0, z_0) = [x_0, A(x_0) \cos(2\pi(x_0 - ct)/\lambda), A(x_0) \sin(2\pi(x_0 - ct)/\lambda)], \text{ for 3D,} \tag{3}$$

where x_0 is the distance measured from the head of the sperm, y_0 and z_0 are respectively the prescribed displacement of the body in y - and z -directions, $A(x_0)$ is the amplitude, c is the traveling wave phase speed, and λ is the wave length. Three additional non-dimensional numbers are introduced, i.e., non-dimensional amplitude A_m/L , traveling-wave Reynolds number cL/ν and wave number L/λ , where A_m is the maximum or average amplitude. In the cases where the motion is driven by a prescribed function [21] or an internal moment, the traveling wave is used to describe the driving function or moment. If non-Newtonian fluid is considered, extra parameter(s) will be introduced [22,23], and the definition of Reynolds number should be modified. Without loss of generality, we take the power-law fluid as an example [24] of which the dynamic viscosity is

$$\nu = \eta \dot{\gamma}^{n-1}, \tag{4}$$

$$\dot{\gamma} = \sqrt{2E_{ij}E_{ij}}, \tag{5}$$

$$E_{ij} = \frac{1}{2} \left(\frac{\partial u_i}{\partial x_j} + \frac{\partial u_j}{\partial x_i} \right), \tag{6}$$

where η is the power-law consistency index, n is the power-law fluid behavior index, and $\dot{\gamma}$ is the shear rate. It should be noted that the Einstein summation convention is applied in Equation (5). One additional parameter, i.e., n , is introduced. The power-law fluids of $n < 1$, $n > 1$ and $n = 1$ are respectively the shear-thinning, shear-thickening and Newtonian fluids. The definition of Reynolds number is modified to [18,22,25]

$$Re = \frac{U^{2-n}L^n}{\eta}. \tag{7}$$

In addition to the flow regimes and sperm kinematics discussed above, the sperm material properties should be considered in the fluid–structure interaction simulations, e.g., bending rigidity, stretching rigidity, structure damping, and mass [20,21]. Therefore, many methods have been developed to address the fluid–structure interaction of sperm in order to study different aspects involved in this topic. In this paper, we present a review of

the numerical methods used in this topic from an engineering perspective to understand the swimming mechanism of sperm. The earliest simplified theories used to evaluate the forces on the sperm are first introduced. Then the boundary-element method that solves Stokes flow is introduced. Finally, the Cartesian grid based methods are introduced.

The rest of this paper is organized as follows. Section 2 summarizes several simplified theories. The boundary–element method for flagellar propulsion in Stokes flow is introduced in Section 3. Section 4 presents driving-configuration-function model based on immersed boundary method (IBM). An integrative model based on IBM is introduced in Section 5. A Singular-Value Decomposition based on the Generalized Finite Difference method for the simulation of fluid–structure interaction problems in a viscous fluid is discussed in Section 6. Section 7 gives an IBM based on finite difference method. Section 8 proposes an immersed boundary–lattice Boltzmann method based driving moment function. Final conclusions are given in Section 9.

2. Simplified Theories

2.1. Taylor’s Swimming Sheet and Cylinder

Taylor [26] pioneered the hydrodynamic analysis of low-Reynolds-number swimmers. In this model, a flagellum is modeled as a two-dimensional infinite waving sheet and the fluid inertia is neglected. By doing this waving motion, a forward speed U will be produced and will be determined. As the forward velocity is in the opposite direction of the traveling wave, we assume the waving sheet is moving with a velocity of $-U\mathbf{e}_x$. The vertical displacement of the material points is prescribed as

$$y_0 = A \sin [2\pi(x_0 - ct)/\lambda]. \tag{8}$$

Please note that this motion is active. The passive deformation is not considered. The swimmer is only allowed to move in longitudinal direction which is determined by the hydrodynamic force. Using the first-order approximation of $2\pi A/\lambda$, it is found that waves of small amplitude traveling down a sheet do not give rise to propulsive stresses in the surrounding viscous fluid. If the second-order approximation of $2\pi A/\lambda$ is used, a forward speed is obtained,

$$\frac{U}{c} = \frac{2\pi^2 A^2}{\lambda^2} \left(1 - \frac{19}{4} \frac{\pi^2 A^2}{\lambda^2}\right). \tag{9}$$

If the amplitude is much less compared to the wave length, the above equation can be simplified as

$$\frac{U}{c} = \frac{2\pi^2 A^2}{\lambda^2}. \tag{10}$$

The simplified wave theory was further extended to the three-dimensional sperm which was modeled by a waving cylindrical tail [27]. If the waving cylindrical tail makes a two-dimensional traveling wave as described by Equation (8), the forward speed is

$$\frac{U}{c} = \frac{2\pi^2 A^2}{\lambda^2} \frac{K_0(2\pi R/\lambda) - 1/2}{K_0(2\pi R/\lambda) + 1/2} \tag{11}$$

where R is the diameter of the cylindrical tail and K_0 is the modified Bessel function of the second kind. If the motion is a three-dimensional spiral wave, the forward speed is

$$\frac{U}{c} = \frac{4\pi^2 A^2}{\lambda^2} \frac{K_0(2\pi R/\lambda) - 1/2}{K_0(2\pi R/\lambda) + 1/2}. \tag{12}$$

It is found that the forward speed by spiral wave is twice of that generated by a plane traveling wave.

2.2. Resistive Force Theory

The resistive force theory was first developed by Taylor [28] for long and narrow animals, and later was applied by Gray and Hancock [29] to sea-urchin sperm swimming. In this model, the local force on an element δs moving with velocity of (u, v) can be written as

$$\delta T = \delta N_y \sin(\theta) - \delta L_y \cos(\theta), \tag{13}$$

$$\delta D = -(\delta N_x \sin(\theta) + \delta L_x \cos(\theta)), \tag{14}$$

$$\delta L_x = u C_L \cos(\theta) \delta s, \tag{15}$$

$$\delta L_y = v C_L \sin(\theta) \delta s, \tag{16}$$

$$\delta N_x = u C_N \sin(\theta) \delta s, \tag{17}$$

$$\delta N_y = v C_N \cos(\theta) \delta s, \tag{18}$$

where δT and δD are respectively the horizontal forces generated by velocity v and u , δN_y and δL_y are respectively the reactions (by lateral motion v) from the water acting normally and tangentially to the surface of the element, δN_x and δL_x are respectively the reactions (by lateral motion u) from the water acting normally and tangentially to the surface of the element, C_L and C_N are the coefficients of resistance to the surface of the element for a medium of known viscosity, and θ is the angle of inclination of the element to the x -axis. δT and δD are also taken as the thrust and drag, respectively. The diagram illustration of the above mentioned forces can be found in Ref. [29]. The total force will be

$$\int_S (\delta T - \delta D) = 0. \tag{19}$$

If a traveling wave described by Equation (8) is used, a forward speed is obtained by solving Equation (19),

$$\frac{U}{c} = \frac{2\pi^2 A^2}{\lambda^2} \left(\frac{C_N - C_L}{C_L} \right), \tag{20}$$

which is the same as Equation (10) if $C_N = 2C_L$. The details of C_N and C_L can be found in Ref. [29].

These simplified models neglect both fluid and sperm inertial forces. In addition, two-dimensional infinite wave sheet and/or simple kinematics are used. However, they are quite important to understand the fundamental mechanisms of sperm swimming, especially the relationship between average forward speed and traveling wave motion. In order to consider inertial force, complex kinematics, and transient state, numerical methods are required.

2.3. Slender Body Theory

Slender body theory represents a flagellum whose length is much larger than its thickness with an arrangement of Stokeslets and doublets along the centreline of the flagellum [30–32]. It was first developed by Lighthill [30] without the end effects, and extended by Johnson [31] to include the end effects. Johnson and Brokaw [33] showed that the slender body theory is more accurate than the resistive force theory. The fundamental of the slender body theory can be found in Ref. [30] and its implementation can be found in Ref. [32]. Here a brief introduction to the result of spiral flagellar motion without end effects is provided. We rewrite the 3D spiral motion as

$$(x_0, y_0, z_0) = [\alpha s, A_0 \cos(\kappa(s - ct)), A_0 \sin(\kappa(s - ct))], \tag{21}$$

where κ is the wave number, s is the arc length measured along the centreline, and $\alpha = \sqrt{1 - A_0^2 \kappa^2}$. According to the slender body theory, the forwarding velocity is given as

$$U_0 = \frac{h\alpha A_0 \kappa}{4\pi\mu} [-1 - \ln \epsilon - A_1(\alpha)], \tag{22}$$

where h is a constant, $\varepsilon = 5.2a/\lambda$ with a being the radius of the flagellum, and $A_1(\alpha)$ is a function arising from an integral. More details of these parameters are referred to Ref. [30].

3. Boundary-Element Method for Flagellar Propulsion in Stokes Flow

The boundary-element method has been extensively used to study the fluid field and forces induced by flagellar motion in Stokes flow where the fluid inertia is ignorable (see Refs. [19,34–37] for several examples). The fluid dynamics considered is described by

$$\frac{\nabla p}{\rho} = \nu \nabla^2 \mathbf{u}, \quad \nabla \cdot \mathbf{u} = 0. \tag{23}$$

The sperm/flagellar motion including position and velocity can be either described [19,34–36] or obtained from fluid–structure interaction [37]. For the prescribed motion, the position of the swimmer can be written as (see e.g., Ref. [19])

$$\mathbf{R} = (X, Y, Z) = (X, Y(X, t), Z(X, t)), \tag{24}$$

where Y and Z are traveling wave functions. If fluid–structure interaction is considered, Montenegro-Johnson et al. [37] employed the following equation to describe the sperm/flagellar dynamics

$$\mathbf{f}_{vis} = \partial_s(-E\mathbf{X}_{SSS} + M\mathbf{n} + T\mathbf{X}_s), \tag{25}$$

where \mathbf{f}_{vis} is the fluid viscous force, E is the bending rigidity, M is the internal moment, and T is the tension. Compared to the model in Section 8, this model does not consider structure damping. In addition, the internal driving moment appears as the form of M_s in Section 8.

At the fluid–structure interface, the non-slip/non-penetration boundary condition applies, and can be described as

$$\mathbf{u}(\mathbf{x}) = \mathbf{U}(s, t), \quad \text{at } \mathbf{x} = \mathbf{X}(s, t). \tag{26}$$

Note that these equations are applicable to the fluid motion around the micro-organism, where the Reynolds number based on the length of the organism and swimming velocity (including forward speed and lateral vibration speed whichever is larger) is extremely small. The flow solution of Equations (23) and (26) can be obtained by

$$u_j(\mathbf{x}) = \int_S G_{ij}(\mathbf{X}, \mathbf{x}) t_i(X) ds - \int_S H_{ij}(\mathbf{X}, \mathbf{x}) U_i(\mathbf{X}) ds, \tag{27}$$

$$G_{ij}(\mathbf{X}, \mathbf{x}) = \frac{1}{8\pi\rho\nu r} \left(\delta_{ij} + \frac{r_i r_j}{r^2} \right), \tag{28}$$

$$H_{ij}(\mathbf{X}, \mathbf{x}) = -\frac{3}{4\pi\rho\nu r^5} r_i r_j \mathbf{r} \cdot \mathbf{n}, \tag{29}$$

$$\mathbf{r} = \mathbf{X} - \mathbf{x}, \tag{30}$$

$$r^2 = \mathbf{r} \cdot \mathbf{r}, \tag{31}$$

where δ_{ij} is the Kronecker delta, \mathbf{n} is a unit outward normal on the fluid–structure interface, and \mathbf{t} is the traction field that can be obtained by taking \mathbf{x} to a boundary point [19].

The primary advantage of using boundary-element method here is that the dimension of the problem is reduced by one, and thus it reduces the number of algebraic equations and avoids mesh generation for two- and three-dimensional problems. Therefore, this method could save computational cost. However, this method ignores fluid inertia and nonlinearity, and thus the associated phenomena cannot be captured.

4. Driving-Configuration-Function Model Based on IBM

A model with both driving and configuration functions was developed by Fauci and McDonald [21] to study the sperm motility. In this model, the immersed boundary method (IBM) [38–41] was developed to couple the sperm dynamics with the fluid dynamics. Based on this method, the surface force acting on the fluid by the sperm is spread onto the volumetric fluid grids by

$$\mathbf{f}(\mathbf{x}, t) = \int \mathbf{F}(s, t) \delta_D(\mathbf{x} - \mathbf{X}(s, t)) ds, \tag{32}$$

where $\mathbf{F}(s, t)$ is the Lagrangian force density on the fluid, \mathbf{X} is the point on the sperm, and δ_D is Dirac’s delta function. The Lagrangian force at a node i on the sperm is calculated by

$$\mathbf{F}_i = -\frac{\delta E_e}{\delta \mathbf{X}_i}, \tag{33}$$

where E_e is the elastic energy of the sperm model. E_e consists of three parts: cell energy (or head energy) with a prescribed configuration function, flagellum energy with driving function, and joint energy that couples the flagellum to the cell body. Therefore,

$$E_e = E_{cell} + E_{flag} + E_{joint}, \tag{34}$$

where E_{cell} , E_{flag} and E_{joint} are respectively cell energy, flagellum energy and joint energy.

If the cell is divided into m points and the flagellum is divided into $n - m$ points, E_{cell} , E_{flag} and E_{joint} can be written as

$$E_{cell} = \frac{1}{2} S_1 \sum_{k=1}^m [|\mathbf{X}_{k+1} - \mathbf{X}_k| - \Delta s]^2 + \frac{1}{2} S_2 \sum_k^m [\mathbf{n}_z \cdot (\mathbf{X}_{k+1} - \mathbf{X}_k) \times (\mathbf{X}_k - \mathbf{X}_{k-1}) - C_{cell}]^2, \tag{35}$$

$$E_{flag} = \frac{1}{2} S_3 \sum_{k=m+1}^n [|\mathbf{X}_{k+1} - \mathbf{X}_k| - \Delta s]^2 + \frac{1}{2} S_4 \sum_{k=m+2}^{n-1} [\mathbf{n}_z \cdot (\mathbf{X}_{k+1} - \mathbf{X}_k) \times (\mathbf{X}_k - \mathbf{X}_{k-1}) - C_{flag}(k, t)]^2, \tag{36}$$

$$E_{joint} = \frac{1}{2} S_3 [|\mathbf{X}_n - \mathbf{X}_1| - \Delta s]^2 + \frac{1}{2} S_4 [\mathbf{n}_z \cdot (\mathbf{X}_1 - \mathbf{X}_n) \times (\mathbf{X}_n - \mathbf{X}_{n-1}) - C_{flag}(n, t)]^2 + \frac{1}{2} S_5 [(\mathbf{X}_2 - \mathbf{X}_m) \cdot (\mathbf{X}_n - \mathbf{X}_1)]^2 \tag{37}$$

where S_1 and S_2 are respectively the stretching and bending coefficients of the cell, S_3 and S_4 are respectively the stretching and bending coefficients of the flagellum, S_5 is the constant used to force the flagellum orthogonal to the cell body at the point of attachment, C_{cell} and C_{flag} are respectively the prescribed configuration function and driving function, and $\mathbf{n}_z = (0, 0, 1)$. In Equation (35), periodic boundary should be applied, i.e., $\mathbf{X}_0 = \mathbf{X}_m$ and $\mathbf{X}_{m+1} = \mathbf{X}_1$. In Equation (36), the moment free at both ends is applied in the bending energy calculation. The last point \mathbf{X}_n of the flagellum is connected to the first point \mathbf{X}_1 on the cell body by the joint energy (see Equation (37)). The last term of Equation (37) is used to drive an orthogonal connection.

C_{cell} is used to maintain a prescribed shape. For example, a configuration of

$$C_{cell} = -(\Delta s)^2 \sin\left(\frac{2\pi}{m}\right)$$

prescribes an equilibrium configuration of the points along the cell body equally-spaced along a circle of radius $r = \Delta s / (2 \sin^2(\pi/m))$. Coefficients S_1 and S_2 determine how closely the equilibrium configuration is enforced.

$C_{flag}(k, t)$ is chosen so that a sine wave of amplitude $a(k)$ is passed along the flagellum. Because the motion of flagellum includes both passive and active parts, it is hard to generate a specific amplitude profile. In general, $C_{flag}(k, t) = A(k) \sin((s - \omega t) / \lambda)$, where λ is the wave length.

The non-slip/non-penetration boundary condition is achieved by using

$$\mathbf{U}_{org} = \int \mathbf{u}(\mathbf{x}, t) \delta_D(\mathbf{x} - \mathbf{X}_{org}(s, t)) d\mathbf{x}, \quad \frac{\partial \mathbf{X}_{org}}{\partial t} = \mathbf{U}_{org}. \quad (38)$$

The Navier-Stokes equations are solved by using the projection method of Chorin with periodic boundary conditions and the velocity field is solved by an implicit scheme. The implicit method is used for the calculation of Equation (32). Such treatment could enhance the numerical stability. In practice, a few hundred to one thousand time steps per period of undulation should be used; the number of time steps per period of undulation should increase with the undulation amplitude as well.

The major advantage of this method is associated with the driving function C_{flag} used. C_{flag} is actually the prescribed motion in the body-fixed frame of reference, which interacts with the fluid forces. In addition, the fluid inertia and nonlinearity are considered. The internal driving mechanism is unclear in this method. In addition, the structure inertia is not considered.

5. An Integrative Model Based on IBM

An integrative model based on IBM, which considers an axoneme consisting of two microtubules, was developed by Dillon et al. [5,42–44]. In this model, the microtubule is modeled as a pair of filaments with diagonal cross-links. The microtubules are linked by nexins and dyneins (dynamic diagonal elastic links) (see Figure 1).

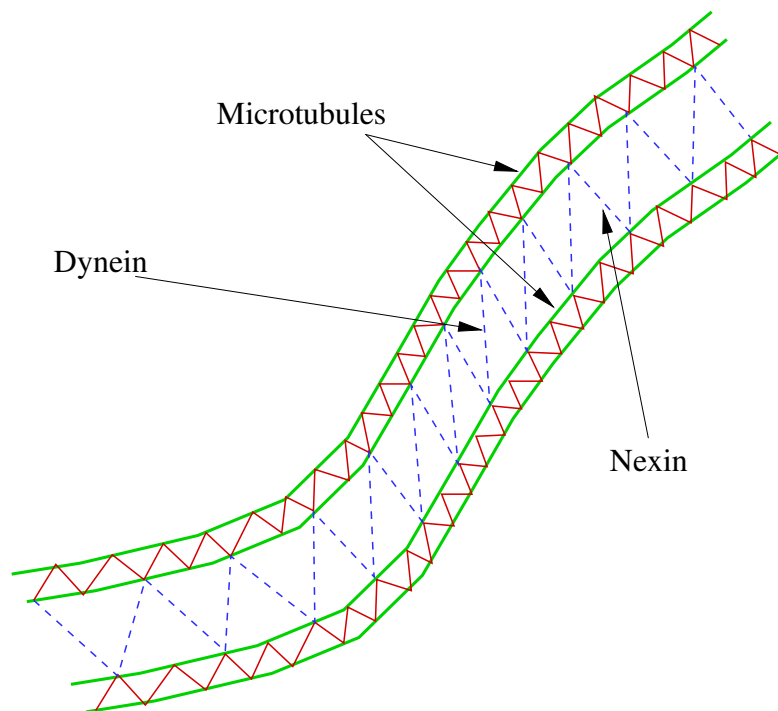


Figure 1. Schematic of a deformed silia in LR (left to right) model.

The immersed boundary method is employed to couple this cilia dynamics with the fluid dynamics. It spreads the surface force onto the volumetric fluid grids in the vicinity of the boundary and treats it as a body force through the following expression

$$\mathbf{f}(\mathbf{x}, t) = \sum_k \int \mathbf{F}^k(s, t) \delta_D(\mathbf{x} - \mathbf{X}^k(s, t)) ds, \tag{39}$$

where $\mathbf{F}^k(s, t)$ is the Lagrangian force density on the fluid by the k -th filament, \mathbf{X}^k is the point on the k -th filament, and δ_D is Dirac’s delta function. The Lagrangian force can be written as

$$\mathbf{F} = \mathbf{F}_M + \mathbf{F}_N + \mathbf{F}_D + \mathbf{F}_C + \mathbf{F}_T, \tag{40}$$

where \mathbf{F}_M is the elastic force arising from the deformation of the microtubules (including contributions from the filaments and the cross links), \mathbf{F}_N is the force caused by the elongation of nexin links, \mathbf{F}_D is induced by the contraction of the dynein links, \mathbf{F}_C is the tethering force to prevent movement of cell wall, and \mathbf{F}_T is the tethering force to prevent movement of the axoneme base.

The microtubule forces at node i of k -th filament is denoted by $\mathbf{F}_{M,i}^k$, and can be written as

$$\mathbf{F}_{M,i}^k = \sum_{ii} -K_{S,i-ii} (||\mathbf{X}_{ii}^k - \mathbf{X}_i^k|| - \Delta s) \frac{\mathbf{X}_i^k - \mathbf{X}_{ii}^k}{||\mathbf{X}_{ii}^k - \mathbf{X}_i^k||}, \tag{41}$$

where ii denotes those points linked to node i by filament segment and the cross-links, $K_{S,i-ii}$ is the stretching coefficient between nodes i and ii , and Δs is the rest length between nodes i and ii . The calculation of \mathbf{F}_N is the same as Equation (41).

\mathbf{F}_D , \mathbf{F}_C and \mathbf{F}_T at node i , denoted by $\mathbf{F}_{X,i}$, can be written as,

$$\mathbf{F}_{X,i} = \sum_{ii} -K_{X,i-ii} (\mathbf{X}_i^k - \mathbf{X}_{ii}^k), \tag{42}$$

where ii denotes those points linked to node i , and $K_{X,i-ii}$ is the stretching coefficient between nodes i and ii .

Dillon et al. [43] also introduced a simple curvature control algorithm to control the flagellar waveform. In this algorithm, individual dyneins are selected from LR (*left to right*) or RL (*right to left*) families at each time step according to the local curvature at the site of the dynein at a time τ_d in the past. The choice of modes is determined by the sign of the lagged local curvature. Initially the shape of the axoneme has a pair of bends, and the resulting bend propagation depends on this curvature control mechanism when the simulation begins. Details of this method can be found in Ref. [43].

The advantage of this method is associated with the facts that it applied curvature control method to achieve swimming motion, and that it includes microtubule structure details, with the cost of algorithm complexity. This method does not consider structure inertia.

6. SVD-GFD Method on a Hybrid Meshfree-Cartesian Grid

In Ref. [45], Yeo et al. presented a Singular-Value Decomposition (SVD) based Generalized Finite Difference (GFD) method for the simulation of fluid–structure interaction problems in a viscous fluid. This method was originally developed for moderate and large Reynolds number swimming problems, e.g., fish swimming and manoeuvring. However, this method can be directly extended to sperm swimming. In this method, computation is carried out on a hybrid grid comprising meshfree nodes around the undulating swimming body which are convected in tandem with the changing shape and motion of the body and Cartesian nodes in the background (as shown in Figure 2). Both types of grids employ the arbitrary Lagrangian–Eulerian (ALE) formulation of the incompressible Navier–Stokes equations to calculate the fluid dynamics

$$\frac{\partial \mathbf{u}}{\partial t} + (\mathbf{u} - \mathbf{u}_g) \cdot \nabla \mathbf{u} = -\frac{\nabla p}{\rho} + \nu \nabla^2 \mathbf{u}, \quad \nabla \cdot \mathbf{u} = 0, \tag{43}$$

where \mathbf{u}_g denotes the convection velocity of the computational grids. At the meshfree nodes and a small number of Cartesian nodes (which contain meshfree nodes in its $[-\Delta x, \Delta x] \times [-\Delta y, \Delta y]$ neighbourhood), derivative approximation is carried out by a GFD scheme that uses the SVD procedure for error minimization [45]. The GFD method is based on the Taylor series approximation where the derivative components $\partial \mathbf{f}_{9 \times 1} = (\partial_x, \partial_y, \partial_{x^2}, \partial_{xy}, \dots, \partial_{y^3})^T f|_{\mathbf{x}_0}$ of a function $f(\mathbf{x})$ at a given position \mathbf{x}_0 are related to its function values $f_i = f(\mathbf{x}_i)$ at n support nodes $\mathbf{x}_i = \mathbf{x}_0 + \Delta \mathbf{x}_i$ by

$$\Delta \mathbf{f}_{n \times 1} = [S]_{n \times 9} \partial \mathbf{f}_{9 \times 1}, \tag{44}$$

$$\Delta \mathbf{f}_{n \times 1} = (f_1 - f_0, f_2 - f_0, \dots, f_n - f_0), \tag{45}$$

$$[S]_{n \times 9} = \begin{bmatrix} \Delta x_1 & \Delta y_1 & \Delta x_1^2/2! & \Delta x_1 \Delta y_1 & \dots & \Delta y_1^3/3! \\ \Delta x_2 & \Delta y_2 & \Delta x_2^2/2! & \Delta x_2 \Delta y_2 & \dots & \Delta y_2^3/3! \\ \vdots & \vdots & \vdots & \vdots & \vdots & \vdots \\ \Delta x_n & \Delta y_n & \Delta x_n^2/2! & \Delta x_n \Delta y_n & \dots & \Delta y_n^3/3! \end{bmatrix}. \tag{46}$$

In general, $n \geq 9$ support nodes are needed to approximate the second-order derivative components of $\partial \mathbf{f}_{9 \times 1}$. The derivatives are obtained as the solution of the over-determined linear system (44) by the method of SVD, which minimizes the ℓ_2 -norm (least square) of the residual error vector.

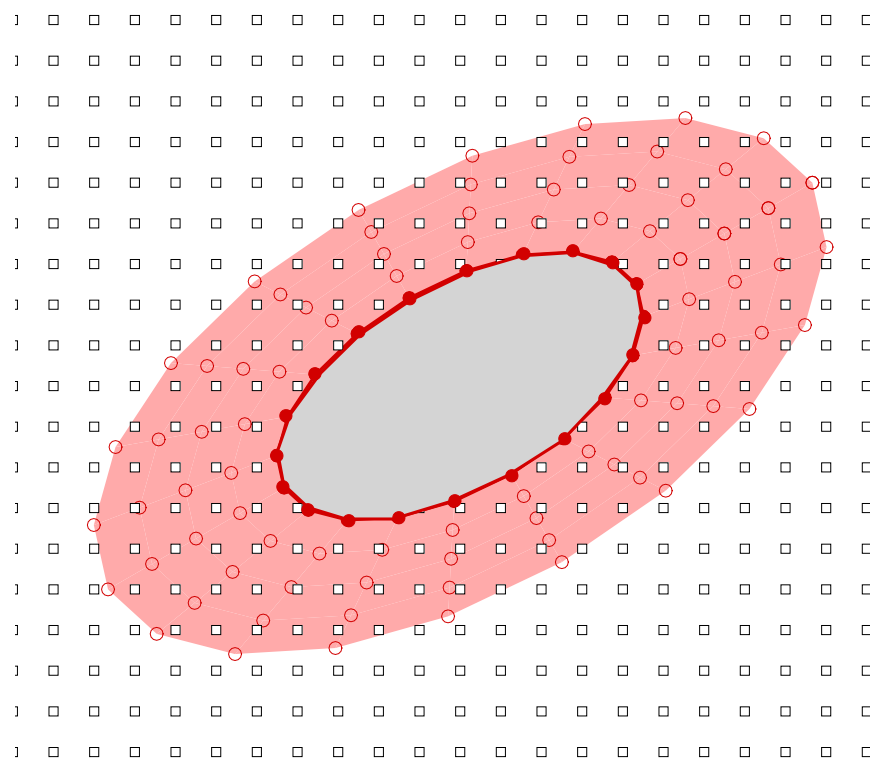


Figure 2. The hybrid meshfree-Cartesian grid in the computational frame: filled circle denotes meshfree body nodes defining the outline of the body; open circle represents the meshfree cloud of nodes enveloping the body; and open square denotes the nodes of Cartesian background.

At other Cartesian nodes which do not contain meshfree nodes in its $[-\Delta x, \Delta x] \times [-\Delta y, \Delta y]$ neighbourhood, traditional finite difference method is used.

Once the fluid dynamics is acquired, the forces on the swimming body can be obtained. Finally, the motion of the body is governed by (also see Ref. [18])

$$m \frac{d\mathbf{V}_c}{dt} = \mathbf{F}_g + \mathbf{F}_f, \tag{47}$$

$$\frac{d(\omega I_c)}{dt} = M_{cf}, \tag{48}$$

$$\mathbf{V}_c = \frac{d\mathbf{X}_c}{dt}, \tag{49}$$

$$\omega = \frac{d\theta}{dt}, \tag{50}$$

where m is the mass of the body, I_c is the moment of inertia about centroid (\mathbf{X}_c) of the body, θ is the orientation angle of the body center line, \mathbf{V}_c is the linear velocity of the mass centroid, ω is the angular velocity of the body, \mathbf{F}_g represents an external force such as gravitational force, \mathbf{F}_f is the fluid forces, and M_{cf} is the fluid moment about centroid. In the body-frame, the body performs motion with prescribed kinematics to achieve cyclic swimming and turning manoeuvres. Similar swimmer dynamics model has been extensively used to study fish-like and sperm-like swimming (see for example Refs. [12,17,20,46]). Equations (47)–(50) governing the centroidal translation and rotation of the swimming body are integrated by a Crank–Nicolson like implicit scheme.

We would like to highlight several major advantages of this method. It combines the advantages of mesh-free discretization for precise definition of bodies and good resolution of boundary regions with the efficiency of standard Cartesian finite difference scheme, so that the interpolation is kept at a very minimal level associated with fresh nodes creation. Furthermore, the density of mesh-free nodes around bodies may be freely varied to give necessary resolution within boundaries. Finally, both meshfree nodes and background Cartesian nodes can be convected if necessary. This will be particularly useful in problems where the swimming body travels over extended distances. Though this method considers structure inertia, it uses the prescribed kinematics, which is not affected by the fluid force, to achieve cyclic swimming and turning manoeuvres.

7. IBM Based on Finite Difference Method

IBM based on finite difference method was extended by Qin et al. [20] to study a small swimmer (e.g., sperm) in a viscous fluid. This method consists of three parts: swimmer dynamics, fluid dynamics and fluid-structure interaction.

In this method, the swimmer dynamics is the same as that used in Refs. [12,17,45], and is described by Equations (47)–(50). Therefore, it will not be repeated here. In the fluid dynamics solver, the fractional step method was adopted to solve the Navier–Stokes Equation (43) without mesh movement (i.e., $\mathbf{u}_g = 0$). Fully implicit time advancement and the Crank–Nicolson scheme were respectively used for the discretization of the diffusion and convection terms on a staggered Cartesian grid. Decoupling of the velocity and pressure was achieved by using a variation of Chorin’s projection method (see Ref. [47] for the details of this method).

The major difference of this method compared to Ref. [45] is that the immersed boundary method is employed to handle the fluid–structure coupling, which spreads the surface force onto the volumetric fluid grids in the vicinity of the boundary and treats it as a body force through the following expression

$$\mathbf{f}(\mathbf{x}, t) = S \text{Re} \int \mathbf{F}(s, t) \delta_D(\mathbf{x} - \mathbf{X}(s, t)) ds, \tag{51}$$

where $S = \rho_s / \rho L$ is the mass ratio (with ρ_s being the structure linear density, ρ being fluid density and L being the swimmer length), Re is the Reynolds number defined by cL / ν (this definition was also used in Ref. [12]), $\mathbf{F}(s, t)$ is the Lagrangian force density on the fluid

by the swimmer body, $\delta_D(\mathbf{x} - \mathbf{X}(\mathbf{s}, t))$ is Dirac's delta function. In this work, the feedback forcing scheme [48–50] is used to calculate the Lagrangian force density, i.e.,

$$\mathbf{F} = \alpha(\mathbf{X} - \mathbf{x}_{ib}) + \beta(\mathbf{U} - \mathbf{u}_{ib}), \tag{52}$$

where α and β are positive constants, \mathbf{U} is the Lagrangian velocity obtained from both prescribed motion, \mathbf{u}_{ib} is the interpolated velocity from flow field according to

$$\mathbf{u}_{ib} = \int \mathbf{u}(\mathbf{x}, t) \delta_D(\mathbf{x} - \mathbf{X}(\mathbf{s}, t)) d\mathbf{x}, \tag{53}$$

and \mathbf{x}_{ib} is the position integrated by using \mathbf{u}_{ib} ,

$$\mathbf{x}_{ib} = \int \mathbf{u}_{ib} dt. \tag{54}$$

In the implementation, Equation (52) is not directly used. Instead, the equations below are used to calculate the Lagrangian force,

$$\Delta\mathbf{X} = \mathbf{X} - \mathbf{x}_{ib}, \tag{55}$$

$$\mathbf{F} = \alpha\Delta\mathbf{X} \left[1 + \frac{\beta}{\alpha\Delta t} \frac{\Delta\mathbf{X}(t) - \Delta\mathbf{X}(t - \Delta t)}{\Delta\mathbf{X}(t)} \right], \tag{56}$$

where the second term of the Lagrangian force is usually less than the first term unless the flagellum shape changes sharply with time or the body swims very fast. This fact is useful for choosing appropriate values of α and β . Details regarding values of α and β can be found in Ref. [47].

Qin et al. [20] applied this method to study a small swimmer (e.g., sperm) in a viscous fluid. They found that for a very small swimmer such as sperm swimming at very low Reynolds numbers, the traveling-wave beating propels the swimmer forward and the asymmetrical parabola beating changes the swimming direction. Similar observation was obtained by the method in Section 8 which applies an internal driving moment to generate the beating motion of a sperm. Qin et al. also found that if the distance between the swimmer and a wall is less than the wavelength, the wall effect on the swimmer motion is strong, which is consistent with fish swimming as discussed in Ref. [51]. Another interesting observation was that the swimmer approaches the wall due to the net torque generated by the non-uniform distribution of the pressure along the flagellum.

Compared to Ref. [45], this method uses IBM, and thus it is more efficient regarding the boundary condition treatment. We also note that an explicit scheme was used in Ref. [20] for equations governing the sperm dynamics, while a Crank–Nicolson like scheme was used in Ref. [45]. Therefore, a much smaller Δt (e.g., 10^{-4}) was used for both structure and fluid dynamics in Ref. [20], while $\Delta t = 10^{-3}$ was used in Ref. [45]. Actually, at each fluid–structure interaction, the integration of structure dynamic equations can be further split into several substeps depending on the stiffness and/or mass ratio, as did in Refs. [52–54]. Similar to the SVD-GFD method on a hybrid meshfree–Cartesian grid in Section 6, this method uses the prescribed kinematics independent of hydrodynamics to achieve cyclic swimming and turning manoeuvres.

8. IB-LBM Based Driving Moment Method

Here we introduce an internal driving nonlinear model based on the immersed boundary–lattice Boltzmann method (IB-LBM) [23,55–61]. In this method, the sperm is simplified as a nonlinear beam. To drive the swimming motion, an internal moment is introduced into the beam equation [59]. Therefore, the geometrically nonlinear motion for the sperm is described as

$$K_v \frac{\partial \mathbf{X}}{\partial t} - \frac{\partial}{\partial s} \left[T(s) \frac{\partial \mathbf{X}}{\partial s} \right] + K_b \frac{\partial^4 \mathbf{X}}{\partial s^4} + \frac{\partial}{\partial s} \left(\frac{\partial M(s, t)}{\partial s} \mathbf{n} \right) = \mathbf{F}_f, \tag{57}$$

where s is the arch length from the leading edge to the tail, $T(s) = K_s(|\frac{\partial \mathbf{x}}{\partial s}| - 1)$ is the stretching stress, K_s is the stretching coefficient, K_b is the bending rigidity, K_v is the damping coefficient, \mathbf{X} is the Lagrangian position vector of the sperm, \mathbf{n} is the normal pointing to the left hand side when s is increasing, $M(s, t)$ is the driving moment, and \mathbf{F}_f is the fluid stress. Both head and tail are shear-free and subjected to driving moment, which can be described by $(\partial^2 \mathbf{X} / \partial s^2)|_{s=0,L} = M(s)$ and $(\partial^3 \mathbf{X} / \partial s^3)|_{s=0,L} = 0$.

The incompressible viscous fluid dynamics is solved by using LBM [62,63] where the kinematics of the fluid is governed by the discrete LBE of a single relaxation time model [55,62–66]

$$g_i(\mathbf{x} + \mathbf{e}_i \Delta t, t + \Delta t) - g_i(\mathbf{x}, t) = -\frac{1}{\tau} [g_i(\mathbf{x}, t) - g_i^{eq}(\mathbf{x}, t)] + \Delta t G_i, \tag{58}$$

where $g_i(\mathbf{x}, t)$ is the distribution function for particles, \mathbf{e}_i is the particle velocity, \mathbf{x} is the position, Δt is the size of the time step, $g_i^{eq}(\mathbf{x}, t)$ is the equilibrium distribution function, τ represents the nondimensional relaxation time, and G_i is the body force term. In the D2Q9 model, the nine possible particle velocities are given by

$$\begin{aligned} \mathbf{e}_0 &= (0, 0), \\ \mathbf{e}_i &= \left(\cos \frac{\pi(i-1)}{2}, \sin \frac{\pi(i-1)}{2} \right) \frac{\Delta x}{\Delta t}, \quad \text{for } i = 1 \text{ to } 4, \\ \mathbf{e}_i &= \left(\cos \frac{\pi(i-9/2)}{2}, \sin \frac{\pi(i-9/2)}{2} \right) \frac{\sqrt{2}\Delta x}{\Delta t}, \quad \text{for } i = 5 \text{ to } 8, \end{aligned}$$

where Δx is the lattice spacing. In Equation (58), g_i^{eq} and G_i are acquired by [64,67]

$$g_i^{eq} = \omega_i \rho \left[1 + \frac{\mathbf{e}_i \cdot \mathbf{u}}{c_s^2} + \frac{\mathbf{u} \mathbf{u} : (\mathbf{e}_i \mathbf{e}_i - c_s^2 \mathbf{1})}{2c_s^4} \right], \tag{59}$$

$$G_i = \left(1 - \frac{1}{2\tau} \right) \omega_i \left[\frac{\mathbf{e}_i - \mathbf{u}}{c_s^2} + \frac{\mathbf{e}_i \cdot \mathbf{u}}{c_s^4} \mathbf{e}_i \right] \cdot \mathbf{f}, \tag{60}$$

where ω_i are the weights given by $\omega_0 = 4/9$, $\omega_i = 1/9$ for $i = 1$ to 4 and $\omega_i = 1/36$ for $i = 5$ to 8 , $\mathbf{u} = (u, v)$ is the velocity of the fluid, $c_s = \Delta x / \sqrt{3} \Delta t$ is the sound speed, and \mathbf{f} is the fluid body force. The relaxation time is related to the fluid kinematic viscosity by

$$\nu = (\tau - 0.5) c_s^2 \Delta t. \tag{61}$$

Finally, the fluid density, velocity and pressure are computed by

$$\rho = \sum_i g_i, \quad \rho \mathbf{u} = \sum_i \mathbf{e}_i g_i + 0.5 \mathbf{f} \Delta t, \quad p = \rho c_s^2. \tag{62}$$

The immersed boundary method is employed to handle the moving boundary, which spreads the surface force onto the volumetric fluid grids in the vicinity of the boundary and treats it as a body force through the following expression

$$\mathbf{f}(\mathbf{x}, t) = \int \mathbf{F}(s, t) \delta_D(\mathbf{x} - \mathbf{X}(s, t)) ds, \tag{63}$$

where $\mathbf{F}(s, t)$ is the Lagrangian force density on the fluid by the elastic boundary, $\delta_D(\mathbf{x} - \mathbf{X}(s, t))$ is Dirac's delta function. The regularized body force is the same as \mathbf{f} in Equation (60), and it enters the kinetic equation of the fluid, Equation (58), through

G_i . Since $\mathbf{F}(s, t)$ is the reaction force of hydrodynamic force on the sperm, \mathbf{F}_f , it can be written as

$$\mathbf{F}(s, t) = -\mathbf{F}_f = \mathbf{F}_v(s, t) + \mathbf{F}_s(s, t) + \mathbf{F}_b(s, t) + \mathbf{F}_d(s, t), \tag{64}$$

$$\mathbf{F}_v(s, t) = -K_v \frac{\partial \mathbf{X}}{\partial t}, \tag{65}$$

$$\mathbf{F}_s(s, t) = \frac{\partial}{\partial s} \left[T(s) \frac{\partial \mathbf{X}}{\partial s} \right], \tag{66}$$

$$\mathbf{F}_b(s, t) = -K_b \frac{\partial^4 \mathbf{X}}{\partial s^4}, \tag{67}$$

$$\mathbf{F}_d(s, t) = -\frac{\partial}{\partial s} \left(\frac{\partial M(s, t)}{\partial s} \mathbf{n} \right). \tag{68}$$

where \mathbf{F}_v , \mathbf{F}_s , \mathbf{F}_b and \mathbf{F}_d are respectively the viscous, stretching, bending, and internal driving forces.

The velocity of a point on the sperm is interpolated from the flow field, and the position of the sperm is updated explicitly by

$$\mathbf{U}(s, t) = \int \mathbf{u}(\mathbf{x}, t) \delta_D(\mathbf{x} - \mathbf{X}(s, t)) d\mathbf{x}, \tag{69}$$

$$\frac{\partial \mathbf{X}(s, t)}{\partial t} = \mathbf{U}(s, t), \tag{70}$$

where $\mathbf{U}(s, t)$ is the velocity of the sperm.

The method ignores the internal structure details and the molecular motor mechanisms of the sperm. Instead, an internal driving moment is employed to drive the swimming motion. By designing a suitable driving moment, one is able to reproduce the traveling wave motion, turning maneuver, and other motions. Furthermore, the structure inertia can be incorporated by using the method in Ref. [55]. In practice, the driven force is sometimes explicitly provided [68,69], i.e., $\mathbf{F}_d(s, t) = \mathbf{F}_{d0}(s) \sin[(s - \omega t)/\lambda]$ where $\mathbf{F}_{d0}(s)$ is the force amplitude. The leading edge trajectory, and speeds in x - and y -directions presented in Ref. [59] are shown in Figure 3. The pressure distributions around a swimming sperm in 2D and 3D space by Liu et al. [69] are shown in Figure 4.

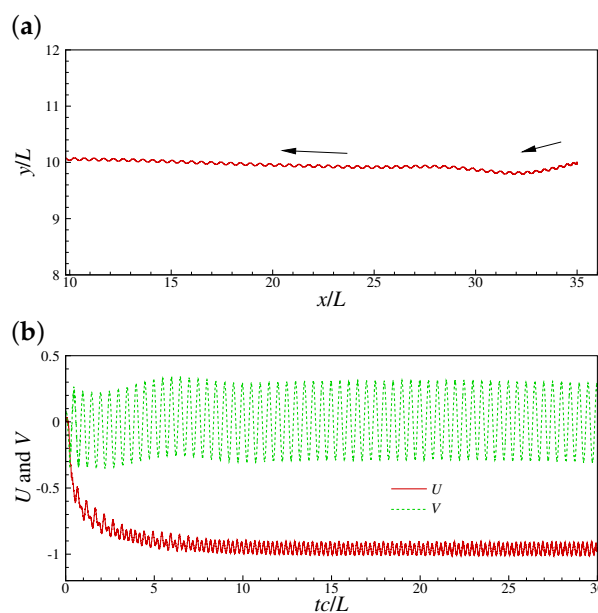


Figure 3. A 2D sperm swimming by the immersed boundary–lattice Boltzmann method (IB-LBM) based driving moment method: (a) Leading edge trajectory, and (b) speeds in x - and y -directions [59].

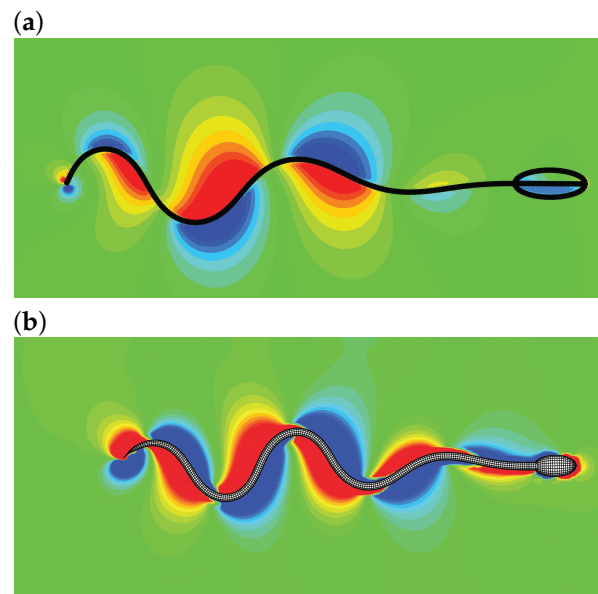


Figure 4. A sperm swimming by the IB-LBM based driving moment method: pressure distribution for 2D (a) and 3D (b) simulations [69].

9. Conclusions

In this article, a number of previous efforts focusing on the theoretical and numerical methods for sperm swimming have been introduced from an engineering perspective. Specifically, the governing equations and parameters for sperm swimming in fluid are first presented and discussed. The simplified theoretical methods, including Taylor's swimming sheet and cylinder, the resistive force theory and the slender body theory, are then introduced. Finally, numerical methods, including boundary-element method for flagellar propulsion in Stokes flow, driving-configuration-function model based on IBM, an integrative model based on IBM, SVD-GFD method on a hybrid meshfree-Cartesian grid, IBM based on finite difference method and IB-LBM based driving moment method, are provided. The methods include IBMs and non-IBMs. IBMs are normally based on the delta function which is a first-order approach in space. The major advantage of these methods is the simplicity in handling boundary conditions at the fluid-structure interacts. For the non-IBMs solving FSI systems, effort is required to handle the computational mesh, bringing benefit of higher accuracy in space.

Actually, among the hundreds of millions of sperm cells that begin the journey up the oviducts, only a few excellent travelers will ever reach their destination. They have to swim in the right direction over distances that are around 1000 times their own length. In addition, they are exposed to complex currents along the way. During their journey, the sperms might explore the hydrodynamic benefits from other sperms around them or the flexible walls so that they have better opportunities to reach the destination. There may be both collaboration and competition between sperms. Therefore, significant work needs to be done to gain better understanding of this complex process. There are several issues for further research in this area.

First, the control strategy of driving moment is an interesting topic considering the "fierce race" during the journey up the oviducts. The complex currents and the moving wall require excellent control strategy which has not been studied. The combination of numerical methods with artificial intelligence, which has been introduced in high-Reynolds-number swimmers [70,71], is an attractive strategy to achieve this. Second, the sperm-sperm and sperm-wall interactions are important during this journey. In previous numerical experiments, it was found that two tandem sperms enjoy benefits from the interaction in terms of acceleration and forward speed. However, instability occurs during the swimming, and thus it may need extra energy for the sperm to recover from instability. In addition, the interaction among large number of sperms and walls is not well understood. The chal-

lenges are the swimming stability, control and the response of the sperm to the complex environments which could be addressed by artificial intelligence. Third, chemotaxis is an important feature of sperms. It is the movement in response to a chemical stimulus from egg (and/or oviduct). Understanding of sperm chemotaxis is of importance to understand its swimming mechanism and driving moment control. Fourth, it is desired to study the non-Newtonian effects on the swimming performance of sperms considering most body fluids behave according to non-Newtonian rheologies which have strong effects on fluid–structure interaction at low Reynolds numbers. Fifth, the beating of the sperm tail is subjected to fluctuations in internal forces due to the noise in the activity of the motors, which could be modelled by Brownian motion [72,73] which should be considered in the numerical modelling. Finally, collaboration and competition between sperms [73], and optimization, also need further study in the modelling.

Author Contributions: Conceptualization, F.-B.T.; methodology, F.-B.T. and L.W.; writing—original draft preparation, F.-B.T. and L.W.; writing—review and editing, F.B.T. and L.W. All authors have read and agreed to the published version of the manuscript.

Funding: We thank Vishal Naidu for collecting some references, drafting several paragraphs and useful discussions. This research was partially funded by Australian Research Council Discovery Early Career Researcher Award (Project No. DE160101098).

Institutional Review Board Statement: Not applicable.

Informed Consent Statement: Not applicable.

Conflicts of Interest: The authors declare no conflict of interest.

References

- Blum, J.J.; Lubliner, J. Biophysics of Flagellar Motility. *Annu. Rev. Biophys. Bioeng.* **1973**, *2*, 181–219. [[CrossRef](#)]
- Brennen, C.; Winet, H. Fluid Mechanics of Propulsion by Cilia and Flagella. *Ann. Rev. Fluid Mech.* **1977**, *9*, 339–398. [[CrossRef](#)]
- Purcell, E.M. Life at low Reynolds number. *Am. J. Phys.* **1977**, *45*, 3–11. [[CrossRef](#)]
- Mortimer, S.T. A critical review of the physiological importance and analysis of sperm movement in mammals. *Hum. Repr. Update* **1997**, *3*, 403–439. [[CrossRef](#)]
- Dillon, R.H.; Fauci, L.J.; Yang, X. Sperm motility and multiciliary beating: An integrative mechanical model. *Comput. Math. Appl.* **2006**, *52*, 749–758. [[CrossRef](#)]
- Lauga, E.; Powers, T.R. The hydrodynamics of swimming microorganisms. *Rep. Prog. Phys.* **2009**, *72*, 096601. [[CrossRef](#)]
- Gaffney, E.A.; Gadêlha, H.; Smith, D.J.; Blake, J.R.; Kirkman-Brown, J.C. Mammalian Sperm Motility: Observation and Theory. *Annu. Rev. Fluid Mech.* **2011**, *43*, 501–528. [[CrossRef](#)]
- Ombelet, W.; Cooke, I.; Dyer, S.; Serour, G.; Devroey, P. Infertility and the provision of infertility medical services in developing countries. *Hum. Repr. Update* **2008**, *14*, 605–621. [[CrossRef](#)]
- Krausz, C. Male infertility: Pathogenesis and clinical diagnosis. *Best Pract. Res. Clin. Endocrinol. Metab.* **2011**, *25*, 271–285. [[CrossRef](#)]
- Lotti, F.; Maggi, M. Ultrasound of the male genital tract in relation to male reproductive health. *Hum. Repr. Update* **2015**, *21*, 56–83. [[CrossRef](#)]
- Giwercman, A.; Carlsen, E.; Keiding, N.; Skakkebaek, N.E. Evidence for Increasing Incidence of Abnormalities of the Human Testis: A Review. *Environ. Health Perspect.* **1993**, *101*, 65–71.
- Tian, F.B.; Lu, X.Y.; Luo, H. Propulsive performance of a body with a traveling wave surface. *Phys. Rev. E* **2012**, *86*, 016304. [[CrossRef](#)] [[PubMed](#)]
- Katz, D.F.; Dott, H.M. Methods of measuring swimming speed of spermatozoa. *J. Reprod. Fert.* **1975**, *45*, 263–272. [[CrossRef](#)] [[PubMed](#)]
- Lauga, E. *Fluid Dynamics of Cell Motility*; Cambridge University: Cambridge, UK, 2020.
- Childress, S. *Mechanics of Swimming and Flying*; Cambridge University Press: New York, NY, USA, 1981.
- Xu, Y.Q.; Tian, F.B.; Tang, X.Y.; Deng, Y.L. A mathematical model for micro- and nan-swimmer. *J. Mech. Med. Biol.* **2013**, *13*, 1340013. [[CrossRef](#)]
- Tian, F.B.; Xu, Y.Q.; Tang, X.Y.; Deng, Y.L. Study on a self-propelled fish swimming in viscous fluid by a finite element method. *J. Mech. Med. Biol.* **2013**, *13*, 1340012. [[CrossRef](#)]
- Deng, H.B.; Xu, Y.Q.; Chen, D.D.; Dai, H.; Wu, J.; Tian, F.B. On numerical modeling of animal swimming and flight. *Comput. Mech.* **2013**, *52*, 1221–1242. [[CrossRef](#)]
- Phan-Thien, N.; Tran-Cong, T.; Ramia, M. A boundary-element analysis of flagellar propulsion. *J. Fluid Mech.* **1987**, *184*, 533–549. [[CrossRef](#)]

20. Qin, F.H.; Huang, W.X.; Sung, H.J. Simulation of small swimmer motions driven by tail/flagellum beating. *Comput. Fluids* **2012**, *55*, 109–117. [[CrossRef](#)]
21. Fauci, L.J.; McDonald, A. Sperm motility in the presence of boundaries. *Bull. Math. Biol.* **1995**, *57*, 679–699. [[CrossRef](#)]
22. Tian, F.B.; Bharti, R.P.; Xu, Y.Q. Deforming-Spatial-Domain/Stabilized Space-Time (DSD/SST) method in computation of non-Newtonian fluid flow and heat transfer with moving boundaries. *Comput. Mech.* **2014**, *53*, 257–271. [[CrossRef](#)]
23. Ma, J.; Wang, Z.; Young, J.; Lai, J.C.S.; Sui, Y.; Tian, F.B. An immersed boundary–lattice Boltzmann method for fluid–structure interaction problems involving viscoelastic fluids and complex geometries. *J. Comput. Phys.* **2020**, *415*, 109487. [[CrossRef](#)]
24. Chhabra, R.P.; Richardson, J.F. *Non-Newtonian Flow and Applied Rheology*, 2nd ed.; Butterworth-Heinemann: Oxford, UK, 2008.
25. Tian, F.B. Deformation of a capsule in a power-law shear flow. *Comput. Math. Meth. Med.* **2016**, *2016*, 7981386. [[CrossRef](#)]
26. Taylor, G. Analysis of the swimming of microscopic organisms. *Proc. R. Soc. Lond. A* **1951**, *209*, 447–461.
27. Taylor, G. The action of waving cylindrical tails in propelling microscopic organisms. *Proc. R. Soc. Lond. A* **1952**, *211*, 225–239.
28. Taylor, G. Analysis of the swimming of long and narrow animals. *Proc. R. Soc. Lond. A* **1952**, *214*, 158–183.
29. Gray, J.; Hancock, G.J. The Propulsion of Sea-Urchin Spermatozoa. *J. Exp. Biol.* **1955**, *32*, 802–814.
30. Lighthill, J. Flagellar Hydrodynamics. *SIAM Rev.* **1976**, *18*, 161–230. [[CrossRef](#)]
31. Johnson, R.E. An improved slender-body theory for Stokes flow. *J. Fluid Mech.* **1980**, *99*, 411–431. [[CrossRef](#)]
32. Rodenborn, B.; Chen, C.H.; Swinney, H.L.; Liu, B.; Zhang, H.P. Propulsion of microorganisms by a helical flagellum. *Proc. Natl. Acad. Sci. USA* **2013**, *110*, E338–E347. [[CrossRef](#)]
33. Johnson, R.E.; Brokaw, C.J. Flagellar hydrodynamics. A comparison between resistive-force theory and slender-body theory. *Biophys. J.* **1979**, *25*, 113–127. [[CrossRef](#)]
34. Smith, D.J. A boundary element regularized Stokeslet method applied to cilia- and flagella-driven flow. *Proc. R. Soc. Lond. A* **2009**, *465*, 3605–3626. [[CrossRef](#)]
35. Liu, B.; Powers, T.R.; Breuer, K.S. Force-free swimming of a model helical flagellum in viscoelastic fluids. *Proc. Natl. Acad. Sci. USA* **2011**, *108*, 19516–19520. [[CrossRef](#)]
36. Ishimoto, K.; Gaffney, E.A. A study of spermatozoan swimming stability near a surface. *Proc. R. Soc. Lond. A* **2014**, *360*, 187–199. [[CrossRef](#)]
37. Montenegro-Johnson, T.D.; Gadêlha, H.; Smith, D.J. Spermatozoa scattering by a microchannel feature: An elasto-hydrodynamic model. *R. Soc. Open Sci.* **2015**, *2*, 140475. [[CrossRef](#)]
38. Peskin, C.S. Flow patterns around heart valves: A numerical method. *J. Comput. Phys.* **1972**, *10*, 252–271. [[CrossRef](#)]
39. Peskin, C.S. The immersed boundary method. *Acta Numer.* **2002**, *11*, 479–517. [[CrossRef](#)]
40. Mittal, R.; Iaccarino, G. Immersed boundary method. *Annu. Rev. Fluid Mech.* **2005**, *37*, 239–261. [[CrossRef](#)]
41. Huang, W.X.; Tian, F.B. Recent trends and progress in the immersed boundary method. *Inst. Mech. Eng. C J. Mech. Eng. Sci.* **2019**, *233*, 7617–7636. [[CrossRef](#)]
42. Dillon, R.H.; Fauci, L.J. An integrative model of internal axoneme mechanics and external fluid dynamics in ciliary beating. *J. Theor. Biol.* **2000**, *207*, 415–430. [[CrossRef](#)] [[PubMed](#)]
43. Dillon, R.H.; Fauci, L.J.; Omoto, C. Mathematical modeling of axoneme mechanics and fluid dynamics in ciliary and sperm motility. *Dyn. Cont. Disc. Impul. Sys. Ser. A* **2003**, *10*, 745–757.
44. Dillon, R.H.; Fauci, L.J.; Omoto, C.; Yang, X. Fluid dynamic models of flagellar and ciliary beating. *Annu. N. Y. Acad. Sci.* **2007**, *1101*, 494–505. [[CrossRef](#)]
45. Yeo, K.S.; Ang, S.J.; Shu, C. Simulation of fish swimming and manoeuvring by an SVD–GFD method on a hybrid meshfree–Cartesian grid. *Comput. Fluids* **2010**, *39*, 403–430. [[CrossRef](#)]
46. Carling, J.; Williams, T.L.; Bowtell, G. Self-propelled anguilliform swimming: Simultaneous solution of the two-dimensional Navier–Stokes equations and Newton’s laws of motion. *J. Exp. Biol.* **1998**, *201*, 3143–3166. [[PubMed](#)]
47. Huang, W.X.; Sung, H.J. An immersed boundary method for fluid–flexible structure interaction. *Comput. Meth. Appl. Mech. Eng.* **2009**, *198*, 2650–2661. [[CrossRef](#)]
48. Goldstein, D.; Handler, R.; Sirovich, L. Modeling a no-slip flow boundary with an external force field. *J. Comput. Phys.* **1993**, *105*, 354–366. [[CrossRef](#)]
49. Saiki, E.M.; Biringen, S. Numerical simulation of a cylinder in uniform flow: Application of a virtual boundary method. *J. Comput. Phys.* **1996**, *123*, 450–465. [[CrossRef](#)]
50. Fadlun, E.A.; Verzicco, R.; Orlandi, P.; Mohd-Yusof, J. Combined immersed-boundary finite-difference methods for three-dimensional complex flow simulations. *J. Comput. Phys.* **2003**, *161*, 35–60. [[CrossRef](#)]
51. Dong, G.J.; Lu, X.Y. Characteristics of flow over traveling-wavy foils in a side-by-side arrangement. *Phys. Fluids* **2007**, *19*, 057107. [[CrossRef](#)]
52. Tian, F.B.; Dai, H.; Luo, H.; Doyle, J.F.; Rousseau, B. Fluid–structure interaction involving large deformations: 3D simulations and applications to biological systems. *J. Comput. Phys.* **2014**, *258*, 451–469. [[CrossRef](#)]
53. Tian, F.B. FSI modeling with the DSD/SST method for the fluid and finite difference method for the structure. *Comput. Mech.* **2014**, *54*, 581–589. [[CrossRef](#)]
54. Tian, F.B.; Wang, Y.; Young, J.; Lai, J.C.S. An FSI solution technique based on the DSD/SST method and its applications. *Math. Model. Meth. Appl. Sci.* **2015**, *25*, 2257–2285. [[CrossRef](#)]

55. Tian, F.B.; Luo, H.; Zhu, L.; Liao, J.C.; Lu, X.Y. An immersed boundary-lattice Boltzmann method for elastic boundaries with mass. *J. Comput. Phys.* **2011**, *230*, 7266–7283. [[CrossRef](#)]
56. Xu, Y.Q.; Tian, F.B.; Li, H.J.; Deng, Y.L. Red blood cell partitioning and blood flux redistribution in microvascular bifurcation. *Theor. Appl. Mech. Lett.* **2012**, *2*, 024001. [[CrossRef](#)]
57. Tian, F.B.; Lu, X.Y.; Luo, H. Onset of instability of a flag in uniform flow. *Theor. Appl. Mech. Lett.* **2012**, *2*, 022005. [[CrossRef](#)]
58. Xu, Y.Q.; Tian, F.B.; Deng, Y.L. An efficient red blood cell model in the frame of IB-LBM and its application. *Int. J. Biomath.* **2013**, *6*, 1250061. [[CrossRef](#)]
59. Tian, F.; Young, J.; Lai, J. An immersed boundary-lattice Boltzmann method for swimming sperms. In Proceedings of the 20th Australasian Fluid Mechanics Conference, AFMC 2016, Perth, Australia, 5–8 December 2016; p. 436.
60. Xu, L.; Tian, F.B.; Young, J.; Lai, J.C.S. A novel geometry-adaptive Cartesian grid based immersed boundary-lattice Boltzmann method for fluid-structure interactions at moderate and high Reynolds numbers. *J. Comput. Phys.* **2018**, *375*, 22–56. [[CrossRef](#)]
61. Wang, L.; Tian, F.B. Numerical simulation of flow over a parallel cantilevered flag in the vicinity of a rigid wall. *Phys. Rev. E* **2019**, *99*, 053111. [[CrossRef](#)] [[PubMed](#)]
62. Chen, S.; Doolen, G.D. Lattice Boltzmann method for fluid flows. *Annu. Rev. Fluid Mech.* **1998**, *30*, 329–364. [[CrossRef](#)]
63. Aidun, C.K.; Clausen, J.R. Lattice-Boltzmann method for complex flows. *Annu. Rev. Fluid Mech.* **2010**, *42*, 439–472. [[CrossRef](#)]
64. Wu, J.; Shu, C. Implicit velocity correction-based immersed boundary-lattice Boltzmann method and its applications. *J. Comput. Phys.* **2009**, *228*, 1963–1979. [[CrossRef](#)]
65. Tian, F.B.; Luo, H.; Zhu, L.; Lu, X.Y. Interaction between a flexible filament and a downstream rigid body. *Phys. Rev. E* **2010**, *82*, 026301. [[CrossRef](#)]
66. Tian, F.B. Role of mass on the stability of flag/flags in uniform flow. *Appl. Phys. Lett.* **2013**, *103*, 034101. [[CrossRef](#)]
67. Guo, Z.L.; Zheng, C.G.; Shi, B.C. Discrete lattice effects on the forcing term in the lattice Boltzmann method. *Phys. Rev. E* **2002**, *65*, 046308. [[CrossRef](#)]
68. Xu, Y.Q.; Wang, M.Y.; Liu, Q.Y.; Tang, X.Y.; Tian, F.B. External force-induced focus pattern of a flexible filament in a viscous fluid. *Appl. Math. Model.* **2018**, *53*, 369–383. [[CrossRef](#)]
69. Liu, Q.Y.; Tang, X.Y.; Chen, D.D.; Xu, Y.Q.; Tian, F.B. Hydrodynamic study of sperm swimming near a wall based on the immersed boundary-lattice Boltzmann method. *Eng. Appl. Comput. Fluid Mech.* **2020**, *14*, 853–870. [[CrossRef](#)]
70. Verma, S.; Novati, G.; Koumoutsakos, P. Efficient collective swimming by harnessing vortices through deep reinforcement learning. *Proc. Natl. Acad. Sci. USA* **2018**, *115*, 5849–5854. [[CrossRef](#)] [[PubMed](#)]
71. Zhu, Y.; Tian, F.B.; Young, J.; Liao, J.C.; Lai, J.C.S. A numerical study of fish adaption behaviors in complex environments with a deep reinforcement learning and immersed boundary-lattice Boltzmann method. *Sci. Rep.* **2021**, *11*, 1691. [[CrossRef](#)]
72. Elgeti, J.; Gompper, G. Wall accumulation of self-propelled spheres. *Europhys. Lett.* **2013**, *101*, 48003. [[CrossRef](#)]
73. Fisher, H.S.; Giomi, L.; Hoekstra, H.E.; Mahadevan, L. The dynamics of sperm cooperation in a competitive environment. *Proc. R. Soc. B Biol. Sci.* **2014**, *281*, 20140296. [[CrossRef](#)]